RESEARCH ARTICLE | AUGUST 10 2026

Understanding intrinsic loss in thin-film lithium niobate ring resonators via adiabatic coupling

Special Collection: Thin-film lithium niobate for integrated photonics

Xinrui Zhu ; Hana K. Warner ; Yunxiang Song ; Donald Witt ; Marko Lončar

APL Photonics 11, 086110 (2026)
https://doi.org/10.1063/5.0338197

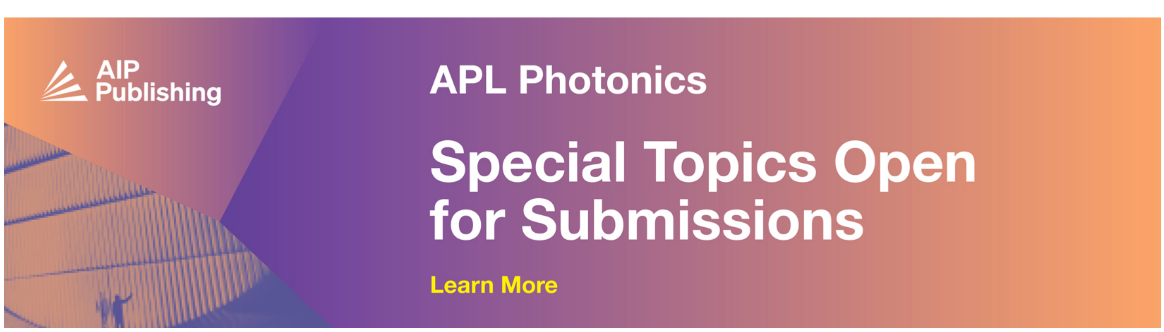

APL Photonics ARTICLE pubs.aip.org/aip/app

Understanding intrinsic loss in thin-film lithium niobate ring resonators via adiabatic coupling

Cite as: APL Photon. 11, 086110 (2026); doi: 10.1063/5.0338197
Submitted: 10 April 2026 • Accepted: 25 July 2026 •
Published Online: 10 August 2026

Xinrui Zhu,[1,a)] Hana K. Warner,[1] Yunxiang Song,[1,2] Donald Witt,[1] and Marko Lončar[1,b)]

AFFILIATIONS

[1] Harvard John A. Paulson School of Engineering and Applied Sciences, Harvard University, Cambridge, Massachusetts 02138, USA
[2] Quantum Science and Engineering, Harvard University, Cambridge, Massachusetts 02138, USA

Note: This paper is part of the Special Topic on Thin-Film Lithium Niobate for Integrated Photonics.

[a)]**Author to whom correspondence should be addressed:** xzhu@g.harvard.edu
[b)]**Electronic mail:** loncar@g.harvard.edu

ABSTRACT

Thin-film lithium niobate (TFLN) has emerged as a versatile integrated photonics platform, combining strong electro-optic and nonlinear effects. Among TFLN devices, ring resonators play a central role in filtering, modulation, and nonlinear optical processes. However, intrinsic loss—which ultimately limits ring performance—is most often summarized by single-valued metrics, and its statistical variability across resonances has received limited attention. Here, we show that intrinsic loss rates in monolithic TFLN ring resonators follow a statistical distribution, comprising a baseline loss and a tail arising from discrete loss events. This behavior is revealed by characterizing 2233 resonances, using an adiabatic waveguide-ring coupling architecture that selectively excites the fundamental mode and yields clean spectra in the ultrahigh-Q_i regime. We find the most probable intrinsic loss rate $\kappa_i = 2\pi \times 10.4$ MHz, indicating operation in a low-loss regime comparable to state-of-the-art thick silicon nitride platforms.

I. INTRODUCTION

Thin-film lithium niobate (TFLN) has rapidly advanced as a leading platform for integrated photonics, combining high electro-optic efficiency with strong second-order nonlinearities.[1–3] This combination has enabled broadband modulation,[4,5] coherent signal transduction,[6,7] frequency conversion,[8,9] and chip-scale microcomb generation,[10–13] positioning TFLN as a key platform for classical and quantum photonic technologies.[14,15] For many of these applications, ring resonators serve as a central building block,[16–18] where the enhancement of circulating optical fields enables compact and efficient optical filtering, modulation, and nonlinear interactions on a chip.

Previous studies of TFLN ring resonators have explored different strategies to maximize intrinsic quality factor (Q_i). For example, increasing the waveguide width has been shown to reduce optical mode overlap with sidewall roughness, thereby suppressing scattering-related loss.[18] Using this approach, Q_i up to ~2.9×10^7 have been demonstrated in wide-waveguide TFLN ring resonators. However, previously used coupling schemes often either excite multiple mode families in the resonator or require local narrowing of the waveguide width at the coupling region.[18,19] Here, we introduce an adiabatic coupling architecture that enables selective excitation of the fundamental mode while preserving a wide, low-scattering waveguide geometry throughout the entire ring,[20] thereby enabling access to clean spectra in the ultrahigh-Q_i regime.

Analyzing a large ensemble of intrinsic loss data (2233 resonances), we observe that intrinsic loss exhibits a statistical distribution, consisting of a Gaussian-like baseline and a tail associated with discrete loss events. This perspective provides a complementary framework for understanding resonance-to-resonance intrinsic loss variation in ring resonators by explicitly characterizing the statistical structure of the loss distribution. Furthermore, the most probable intrinsic loss rate extracted from this ensemble, $\kappa_i = 2\pi \times 10.4$ MHz (corresponding to $Q_i \sim 1.9 \times 10^7$), indicates that thin-film lithium niobate operates in a low-loss regime comparable to state-of-the-art thick silicon nitride platforms.

II. RING RESONATORS AND LOSS MECHANISMS

In this work, we employ a racetrack resonator geometry, a common variant of ring resonators with straight sections, as shown in Fig. 1(a). By forming a closed waveguide loop, optical fields that satisfy the resonance condition can be coherently stored inside the cavity, thereby enhancing light–matter interactions on the chip.[21,22] The total energy decay rate of the cavity is typically given by

$$\kappa = \kappa_i + \kappa_e, \tag{1}$$

where κ_i denotes the intrinsic loss rate associated with propagation inside the ring, and κ_e denotes the coupling rate between the ring and the bus waveguide. The corresponding quality factors are defined as

$$Q = \frac{\omega_0}{\kappa}, \qquad Q_i = \frac{\omega_0}{\kappa_i}, \qquad Q_e = \frac{\omega_0}{\kappa_e}, \tag{2}$$

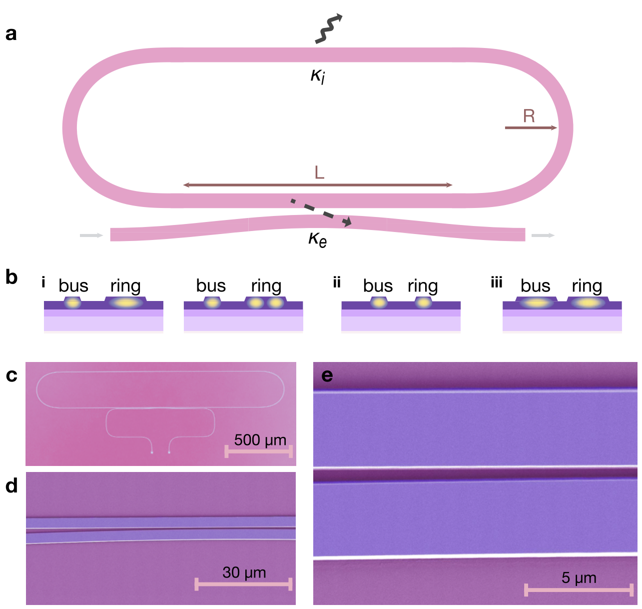

FIG. 1. Mode-selective coupling in thin-film lithium niobate (TFLN) ring resonators. (a) Schematic of a bus-coupled racetrack resonator. The straight-section length (L) and bend radius (R) define the resonator geometry. The intrinsic loss and external coupling rates are denoted by κ_i and κ_e, respectively. (b) Three representative coupling strategies. In conventional approaches, light from a single-mode bus waveguide is either (i) coupled into a wide, multimode ring, thereby exciting multiple modes, or (ii) the ring is tapered to a single-mode width in the coupling region, which can introduce additional scattering loss. In this work (iii), we use a wide, low-loss bus waveguide and ring resonator but introduce an adiabatic coupler that gradually bends the bus waveguide toward the ring, enabling excitation of only the fundamental mode while preserving the wide ring geometry. (c) Optical microscope image of a fabricated racetrack resonator incorporating an adiabatic coupling region for selective fundamental-mode excitation. (d) False-colored scanning electron microscope (SEM) image of the coupling region. (e) Zoomed-in SEM image of the coupling gap.

where ω_0 is the resonance angular frequency. These provide a convenient, dimensionless parameterization of the cavity loss channels. In our discussion, Q_i and κ_i are used interchangeably to describe the same physical loss process, while all statistical analyses are performed in terms of κ_i.

To identify the origins of intrinsic propagation loss, we consider two dominant loss mechanisms. The first mechanism is absorption loss, in which optical energy is irreversibly dissipated as heat within the material. In this work, we consider only linear material absorption under low-power operation, where nonlinear optical loss mechanisms in TFLN are negligible.[23,24] The absorption strength is determined by the imaginary part of the refractive index of the constituent layers (e.g., the LN device layer, the underlying SiO_2 layer, and various interface layers) and may be mitigated through material and structural engineering.

The second mechanism is scattering loss, in which optical energy is coupled into radiation modes or unwanted higher-order modes and is effectively lost. This scattering typically arises from nanoscale roughness at etched sidewalls and waveguide surfaces, as well as from other perturbations to the optical mode. It is strongly dependent on the mode field distribution and, therefore, can be engineered through careful waveguide geometry design and fabrication optimization. In particular, the coupling region is an important site for such scattering pathways. As light transfers between the bus waveguide and the ring, geometric or refractive-index perturbations can cause mode mismatch, introducing an additional parasitic loss channel that contributes to the intrinsic loss rate κ_i rather than the extrinsic coupling rate κ_e. Previous studies have suggested that material absorption contributes only a small fraction of the total intrinsic loss in current TFLN ring resonators, leaving scattering as the dominant loss mechanism.[17,19]

A common strategy to suppress scattering loss in TFLN ring resonators is to employ a wide waveguide for the ring, where the fundamental mode is positioned away from the etched sidewalls. This design minimizes the mode overlap with surface roughness and enables ultrahigh intrinsic quality factors (Q_i). However, direct coupling from a single-mode bus waveguide into a wide ring waveguide [Fig. 1(b-i)] can excite multiple mode families.[18] A workaround is to locally narrow both the bus and the ring waveguides in the coupling region to enforce single-mode coupling [Fig. 1(b-ii)]. This narrowing increases the mode overlap with the sidewalls, which can, in principle, reintroduce scattering loss and limit the achievable Q_i.[19,25]

In this work, we preserve the wide-waveguide geometry of the ring to maintain its low-scattering advantage [Fig. 1(b-iii)].[20] By introducing an adiabatic bend, the bus waveguide remains effectively single-mode in the coupling region, selectively exciting only the fundamental mode of the ring. This design enables clean single-mode resonance spectra and ultrahigh intrinsic quality factors, uniting the benefits of both low scattering and mode selectivity.

III. DEVICE DESIGN AND CHARACTERIZATION

Our devices employ a racetrack resonator geometry with Euler bends of radius 120 μm, as illustrated in Fig. 1(c). The waveguide width is 3 μm, and the straight section length is 1.4 mm, corresponding to a free spectral range (FSR) of ~33 GHz. Compared with our previous ultra-large rings with an FSR of around 6 GHz (4.5 μm waveguide width, 1 cm straight-section length, 200 μm bending

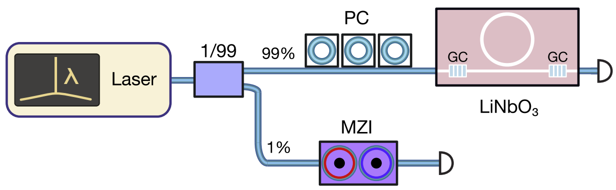

FIG. 2. Measurement setup. A tunable laser is split using a 1/99 splitter, where the 99% arm is sent through a polarization controller (PC) to the device under test, and the 1% arm is routed to a Mach–Zehnder interferometer (MZI) to generate calibration fringes for wavelength referencing. Grating couplers (GCs) were used to couple light into and out of the device.

radius, and maximum Q_i of 2.9×10^7),[18] this compact geometry provides a practical balance between propagation loss and overall device footprint.

The devices were fabricated on chips cleaved from 4-inch X-cut TFLN on insulator wafers purchased from NanoLN. The wafer stack consists of a 600 nm device layer bonded to a 4.7 μm thermal SiO_2 layer on a silicon substrate. Waveguide patterns were defined by electron-beam lithography using hydrogen silsesquioxane (HSQ) resist and subsequently transferred into the LN layer by Ar plasma etching. The etch depth is around 325 nm, leaving a 275 nm slab. Post-etch redeposition was removed through a heated SC-1 clean, followed by diluted HF and piranha treatments to ensure surface cleanliness. Finally, the devices were annealed in oxygen at 520 °C for two hours to mitigate plasma-induced damage and reduce optical absorption. This straightforward monolithic process provides a robust and reproducible fabrication approach that has been broadly applied in our TFLN photonic device developments. As shown in Figs. 1(d) and 1(e), SEM micrographs reveal well-defined sidewalls and coupling regions, highlighting the precision and reliability of our fabrication process.

Optical characterization was performed using the setup schematically shown in Fig. 2. Light from a tunable continuous-wave (CW) laser was split: 99% of the power was directed to the TFLN resonator under test, and 1% was routed to a reference Mach–Zehnder interferometer (MZI). On-chip grating couplers (GCs) were used to couple light into and out of the device, with a 3-dB bandwidth of 65 nm centered around 1545 nm. The transmitted light from the resonator was detected by a high-speed photodetector (Newport 1811), while the MZI output provided periodic interference fringes that served as a frequency reference to correct laser sweep nonlinearity. The detector dark voltage was measured under negligible optical input and subsequently subtracted to correct for baseline offsets. With this calibration procedure, transmission spectra were obtained across the 1480–1600 nm wavelength range for all resonators. These calibrated spectra serve as the basis for extracting the intrinsic quality factors used in the following analysis. We note that our calibration procedure does not correct for the grating coupler response.

IV. MODE SELECTION IN ADIABATIC COUPLING

The guiding principle of our coupler design is *adiabaticity*, in which a system evolves gradually enough to remain in its instantaneous eigenstate without inducing unwanted transitions. In the context of integrated photonics, an adiabatic coupler ensures that the optical mode evolves smoothly along the propagation direction, preserving its mode identity and minimizing reflection, scattering, and unintended mode conversion.

The coupler geometry is illustrated in Fig. 3(a). The bus waveguide follows a squared-sinusoidal trajectory, providing a smooth and symmetric variation of the coupling gap with zero slope at both ends to satisfy the adiabatic condition at the boundaries; no claim of global optimality is made for this specific trajectory choice. Before and after the coupling region, the bus waveguide is tapered from a single-mode width of 0.8 μm to 3 μm. Importantly, within the coupling region, both the bus and the ring waveguides have the same 3 μm width, ensuring phase-matched coupling between their fundamental modes while maintaining a gradual modal transition. This configuration is designed to provide minimal perturbation and broad coupling bandwidth.

To investigate the mode behavior in the coupling region, we combined eigenmode analysis with three-dimensional finite-difference time-domain (FDTD) simulations using Tidy3D. As shown in Fig. 3(b), a 3 μm-wide waveguide supports multiple TE_0–TE_2 and TM_0–TM_2 modes. In our experiment, light is injected through a grating coupler designed for TE_0 excitation near 1550 nm, and the optical mode entering the coupling region is, therefore, primarily TE_0. In the simulation, we placed the mode source at the entrance (left side of the bus waveguide) and monitored the mode composition at the exit (right side of the ring waveguide) for different coupling geometries. Mode purity is quantified by the simulated power fraction in TE_0 at the ring-waveguide exit. As shown in Fig. 3(c), shorter coupling lengths ($L = 200$ μm) or excessive lateral offsets ($w = 10$ μm) lead to substantial excitation of higher-order modes, indicating a breakdown of adiabatic mode evolution. In contrast, for longer coupling lengths ($L = 300$ μm) and moderate lateral offsets ($w = 3$–5 μm), the simulated mode profiles remain nearly pure. We note that, in principle, adiabatic mode evolution could also be achieved with larger lateral separations at longer coupling lengths; in this work, however, we focus on compact coupling geometries and do not discuss these extended designs further.

The measurements corroborate the simulation results. Figures 3(d)–3(g) present the transmission spectra of devices with different coupling geometries. The spectra were normalized to facilitate visual comparison across devices. Devices with shorter or more abrupt coupling sections exhibit multiple sets of resonances, reflecting the presence of higher-order mode families. By contrast, devices employing longer and more adiabatic coupling regions show a single, well-defined resonance series with clearly isolated dips, demonstrating that these geometries effectively suppress higher-order mode excitation in the ring. The fundamental-mode family does not imply that every individual resonance is a pure TE_0 eigenstate, as local modal hybridization may occur. A quantitative evaluation supporting the mode purity discussion is detailed in the supplementary material.

Coupling ideality is a figure of merit that quantifies the fraction of optical power transferred into the desired mode rather than being coupled into undesired modes or lost through parasitic channels.[26–28] Notably, single-mode spectra do not necessarily imply ideal coupling. A detailed discussion of the coupling ideality framework is provided in the supplementary material. In the ideal

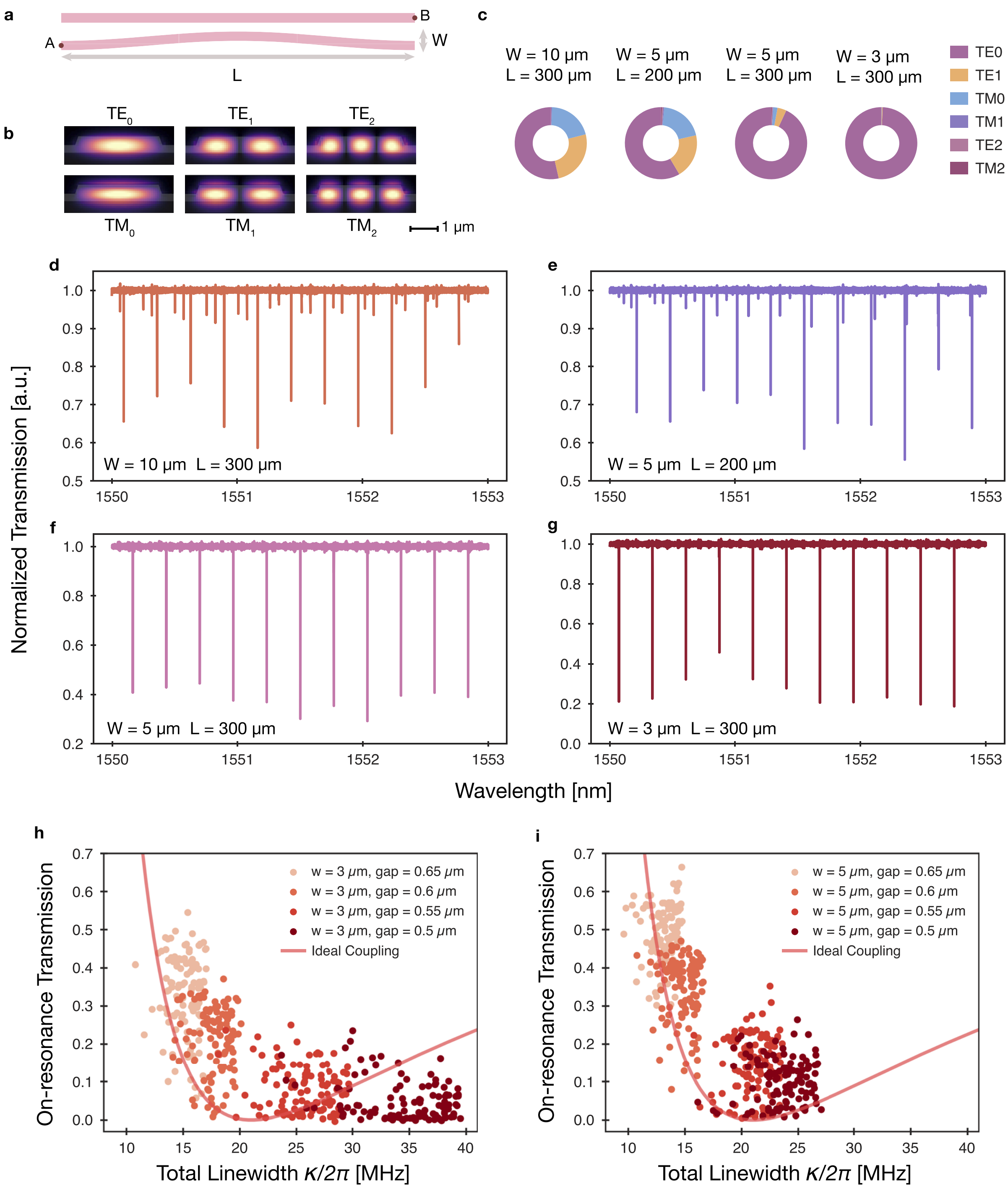

FIG. 3. Mode-selective coupling enabled by an adiabatic coupling geometry. (a) Schematic of the coupling region. The parameter w denotes the lateral offset of the bus-waveguide center between the entrance and the midpoint of the coupling region, and L is the total coupler length. (b) Simulated guided modes supported in a 3 μm-wide TFLN waveguide (TE_0–TE_2 and TM_0–TM_2). (c) Simulated modal power fractions in the ring waveguide for coupling geometries with different (w, L). The fundamental mode is excited at the bus-waveguide entrance [point A in panel (a)], while the mode composition is evaluated at the exit of the ring-waveguide coupling region [point B in panel (a)]. (d)–(g) Normalized transmission spectra measured for the corresponding fabricated devices. (h) and (i) On-resonance transmission vs total linewidth $\kappa/2\pi$ for measured resonances. The solid curve indicates the theoretical linewidth–extinction relation for ideal coupling, assuming an intrinsic loss rate of $\kappa_i/2\pi$ = 10.5 MHz. Scattered points represent experimental data acquired for different coupling gaps in the wavelength range of 1520–1580 nm.

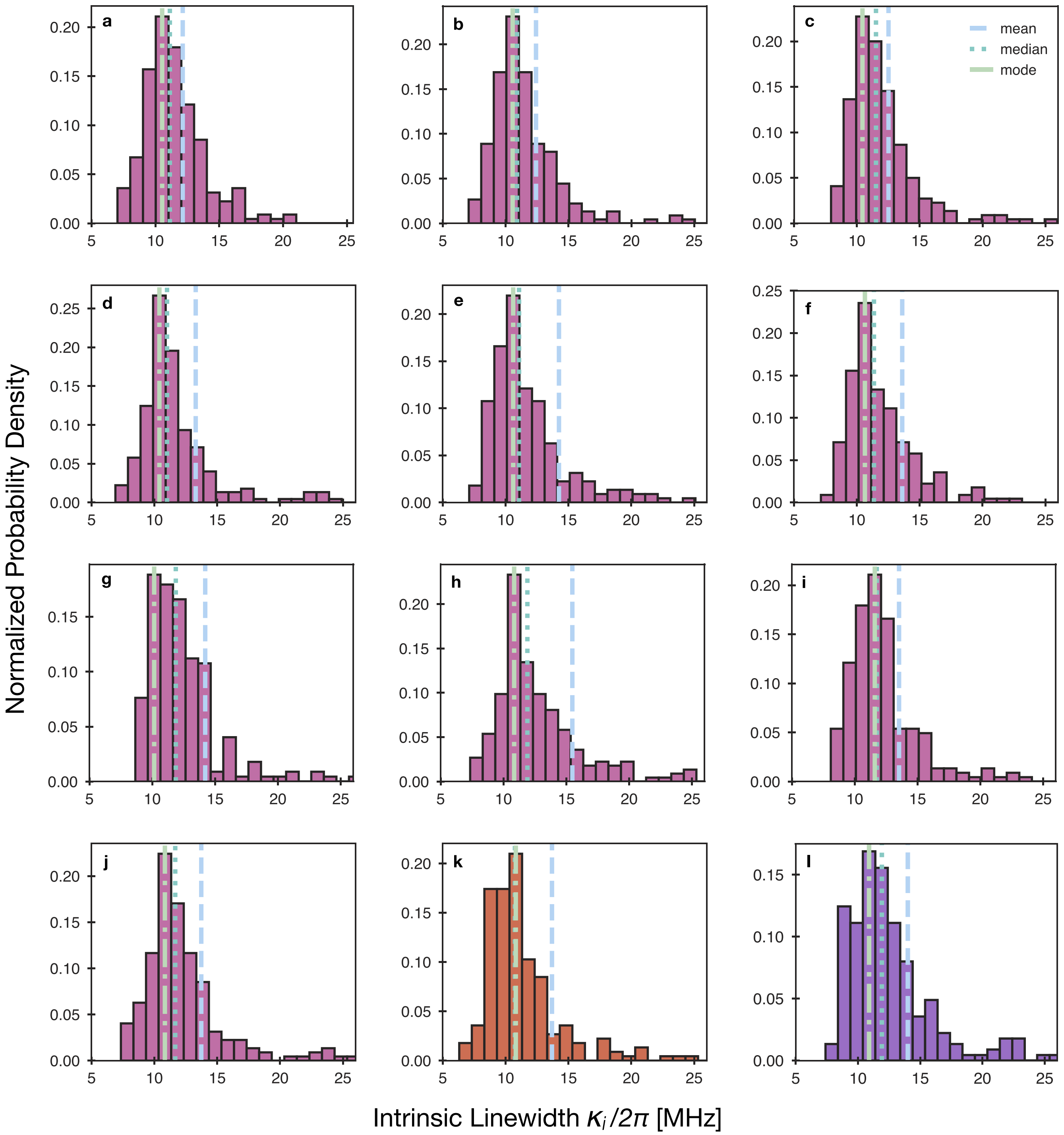

FIG. 4. Statistical distribution of intrinsic loss rates κ_i across multiple resonators. (a)–(l) Normalized histograms of the intrinsic linewidth $\kappa_i/2\pi$ for twelve ring resonators fabricated with the same coupling design (w = 5 μm, L = 300 μm). Resonances within the 1520–1580 nm wavelength range are fitted to obtain κ_i. Vertical lines indicate the mean (light blue, long-dashed), median (teal, dotted), and mode (light green, dashed-dotted) of each device's distribution. The x-axis is fixed from 5 to 26 MHz for consistent comparison. Devices (a)–(j) are fabricated on the same chip, while (k) and (l) are fabricated on two additional chips. The systematic separation between mean, median, and mode across all devices highlights theintrinsic asymmetry of loss.

coupling regime, parasitic loss is negligible, and the relationship between the total resonance linewidth and extinction depth follows the theoretical transmission model, as shown by the solid curves in Figs. 3(h) and 3(i). This behavior exhibits a continuous transition from the under-coupled regime through critical coupling to the over-coupled regime as the coupling strength increases.[27]

We examine the linewidth–extinction relationship for geometries with $L = 300\ \mu$m and $w = 3$–$5\ \mu$m, as shown by the scattered data points in Figs. 3(h) and 3(i). The on-resonance transmission was extracted from the resonance window as $T = T_{\min}/T_{\max}$. Here, $T_{\min}$ and $T_{\max}$ are the minimum and maximum transmission values within the resonance window, respectively. In the presence of

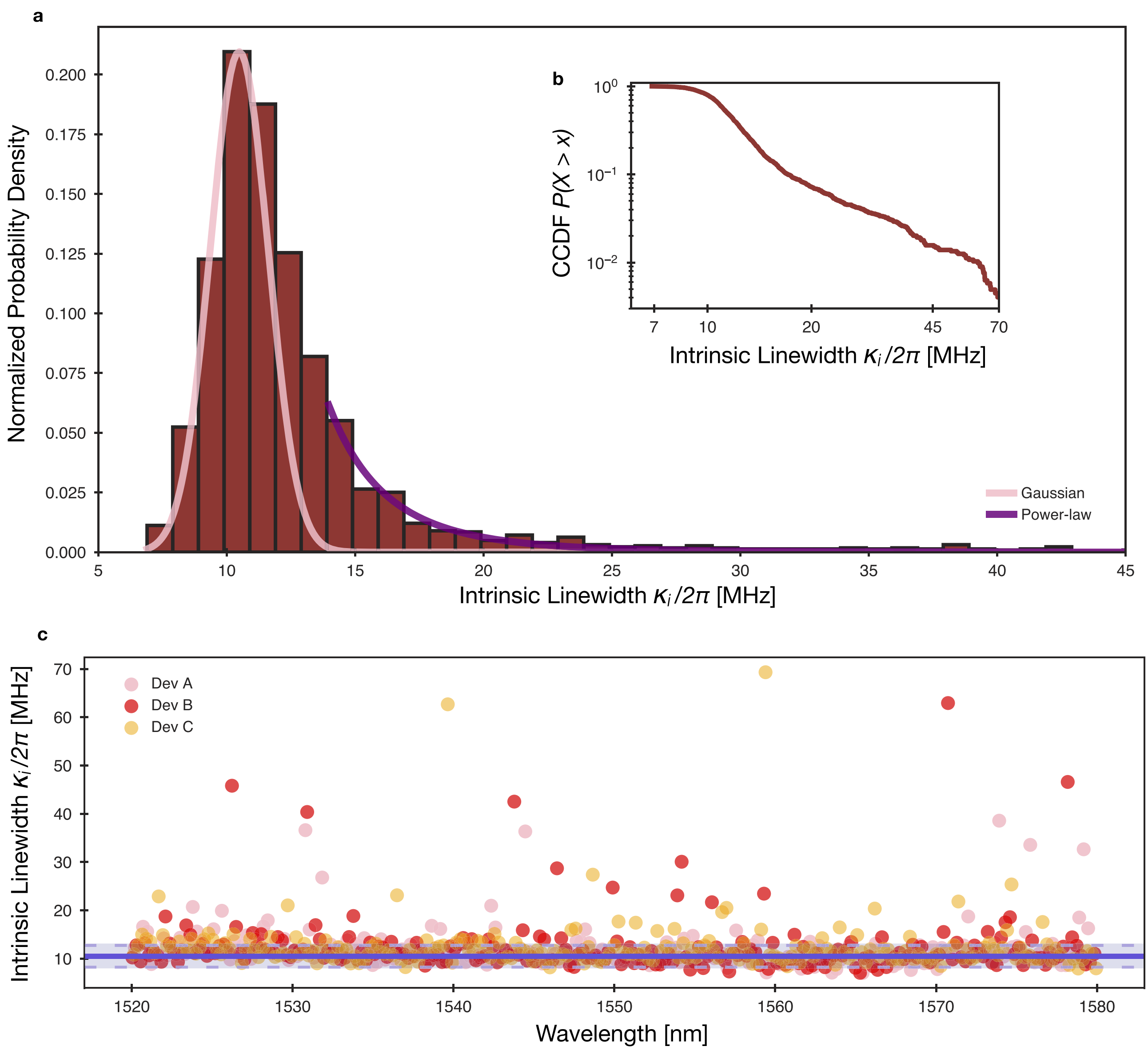

FIG. 5. Statistical characterization and modeling of intrinsic loss. (a) Normalized histogram of intrinsic linewidth $\kappa_i/2\pi$ from ten devices (2233 resonances). The distribution exhibits a Gaussian-like core (pink) together with a truncated power-law-like tail (purple). (b) Complementary cumulative distribution function (CCDF) of the same dataset, showing a deviation from Gaussian behavior in the high-loss regime, with approximately power-law-like decay over an intermediate range followed by a gradual cutoff at large linewidths. (c) Intrinsic linewidth $\kappa_i/2\pi$ vs wavelength for three representative devices [corresponding to devices in Figs. 4(a)–4(c)]. Each point corresponds to a single resonance. The shaded band denotes the Gaussian core $(\mu \pm 2\sigma)$ extracted from the global fit in (a), illustrating that most resonances cluster around the baseline loss, while high-loss events occur sporadically across the wavelength range. For clarity, the histogram is displayed up to $\kappa_i/2\pi = 45$ MHz, and the CCDF is displayed up to $\kappa_i/2\pi = 70$ MHz.

resonance splitting, $T_{\min}$ is taken as the lower of the two split dips. Different coupling gaps probe a range of coupling strengths, and only resonances with κ below the median value are included to isolate intrinsic loss variations. We observe that devices with $w = 3$ μm exhibit deviations from the ideal transmission behavior as the coupling strength increases, particularly for a gap of 0.5 μm. The smaller separation between the bus and ring across the entire coupling region increases sensitivity to fabrication-induced nonuniformities and enhances the integrated mode overlap with parasitic channels. We, therefore, adopt a coupler geometry with $w = 5$ μm for subsequent high-Q_i studies, as it operates farther from the regime where coupling non-ideality begins to dominate.

V. STATISTICAL DISTRIBUTIONS OF INTRINSIC LOSS

To quantify the intrinsic loss rate of our racetrack resonators, we performed a statistical analysis across twelve nominally identical devices sharing the same ring geometry (3 μm waveguide width, 33 GHz FSR) and optimized coupling design ($w = 5$ μm, $L = 300$ μm), as summarized in Fig. 4. Devices (a)–(j) were patterned and processed on the same chip, whereas devices (k) and (l) were fabricated on two additional chips from independent runs, providing a useful check on chip-to-chip reproducibility. To ensure reliable distinction between κ_i and κ_e, we include only devices operating in the moderately under-coupled regime (gaps of ~0.60 – 0.65 μm), where the fits are robust and directly comparable. Resonances within the wavelength range of 1520–1580 nm were included. The complete fitting formalism and representative examples are provided in the supplementary material. This consistently extracted set of intrinsic loss rates provides a solid basis for examining the statistical behavior of intrinsic loss in TFLN ring resonators.

With this dataset in place, we examine the statistical distribution of intrinsic loss rates κ_i across the twelve devices. The intrinsic loss includes contributions from both the straight and bend sections of the racetrack. Because the intrinsic loss exhibits a non-symmetric distribution, single-valued summary statistics are insufficient to characterize device performance. For each device, we extract the mean, median, and mode of the κ_i distribution, as these complementary statistics capture different aspects of the underlying loss behavior. The *mean* intrinsic loss rate reflects the arithmetic average but is strongly influenced by probabilistic, high-loss resonances with exceptionally large κ_i. The *median*, by contrast, is far less sensitive to outliers and provides a more robust indicator of the central behavior of intrinsic loss across a device. The *mode*, defined as the most probable intrinsic loss rate, captures the value most frequently realized across the resonance ensemble. In this work, the mode is taken as the intrinsic loss rate associated with the highest-probability bin of the empirical histogram, using a fixed bin width applied consistently across all devices. Our conclusions are robust under reasonable variations of histogram bin width.

Although each device-level histogram reflects the sensitivity of κ_i to local fabrication variations, aggregating all 2233 resonances from ten devices [Figs. 4(a)–4(j)] from the same chip yields a much smoother distribution that reveals the underlying statistical structure, as shown in Fig. 5(a). This large number of resonances reduces the impact of fabrication variations, as well as measurement and fitting uncertainties. For the aggregated dataset, the mean $\kappa_i/2\pi$ is 13.5 MHz, the median is 11.4 MHz, and the mode is 10.4 MHz. The minimum observed $\kappa_i/2\pi$ is ~7 MHz.

The aggregated linewidth distribution exhibits a Gaussian-like mainlobe together with a truncated power-law tail component [Fig. 5(a)], suggesting the presence of baseline loss and additional high-loss events. The statistical fitting pipeline and robustness validation are presented in the supplementary material.

The Gaussian component reflects the intrinsic baseline loss, arising from many small, uncorrelated contributions such as surface roughness, material absorption, and other minor fabrication- or material-related imperfections. The Gaussian core is centered at $\mu \approx 10.48$ MHz, in close agreement with the most-probable value extracted from the histogram. Since all loss channels contribute positively, any additional mechanism simply adds to the baseline loss and shifts the distribution toward larger linewidths.

The tail portion, by contrast, corresponds to occasional high-loss events. Such discrete events may arise when several factors—including the optical field distribution, local defect configurations, and the possible presence of higher-order or radiation modes at certain wavelengths—coincide in a manner that enhances loss. In realistic devices, the optical fields exhibit frequency-dependent variations both in their transverse profiles and along the ring. Longitudinal spatial variations, in particular, may arise from sidewall roughness and other imperfections that induce backscattering, leading to partially standing-wave-like resonant modes. Consistent with this qualitative interpretation, the complementary cumulative distribution function (CCDF), which directly quantifies the likelihood of observing resonances with intrinsic loss rates exceeding a given threshold, exhibits a power-law-like decay over an intermediate range, followed by a gradual cutoff at large linewidths, as shown in Fig. 5(b).

While the histogram and CCDF summarize the statistics, Fig. 5(c) shows how these mechanisms manifest at the device level. Across three representative resonators, most linewidths lie close to the Gaussian core (shaded region), whereas the high-loss events occur sporadically from resonance to resonance across the wavelength range, consistent with their origin in inherently probabilistic, mode-dependent interactions. This device-level behavior points to a distinction between the factors that set the most probable Q_i and those that determine the average Q_i. Because the latter is shaped strongly by tail events, its improvement is more closely tied to mitigating rare but systematic, conditionally activated loss channels than to further refining the baseline loss—an observation that offers a more general perspective on loss-engineering strategies.

VI. CONCLUSION AND OUTLOOK

We demonstrate ultrahigh-Q_i thin-film lithium niobate (TFLN) ring resonators enabled by an adiabatic coupling architecture that enforces fundamental-mode operation. This design produces clean spectra with robust suppression of higher-order modes, allowing intrinsic loss to be extracted with high confidence across a broad ensemble of resonances. From twelve devices spanning three fabrication runs, we report the mean, median, and most probable intrinsic loss with full statistical transparency for monolithic TFLN. Building on these device-level results, our dataset across 2233 resonances enables a distribution-level description of intrinsic loss in TFLN ring resonators: a Gaussian baseline shaped by numerous small, uncorrelated loss components, overlaid with discrete tail events associated with probabilistically activated loss channels. Although our study was performed on X-cut TFLN, the underlying design principles and loss distribution analysis are expected to be applicable to other TFLN crystal orientations, with the potential to be extended to other integrated photonic platforms.

In addition to recasting loss engineering into a unified physical–statistical perspective, our results place TFLN alongside the leading low-loss integrated photonic platforms. In thick silicon nitride, state-of-the-art intrinsic loss is realized through either Damascene reflow or surface-mechanical polishing, yielding most-probable Q_i values of 3×10^7–4×10^7.[29,30] By comparison, our most-probable Q_i values of $\approx 2 \times 10^7$ are achieved through a straightforward fabrication process.

Looking ahead, the combination of high-Q_i single-mode operation with electro-optic and all-optical nonlinearities opens a broader horizon for integrated photonics in TFLN.

SUPPLEMENTARY MATERIAL

The supplementary material is organized into four parts: (1) the resonance fitting model, (2) quantitative analysis of mode purity, (3) evaluation of coupling ideality, and (4) statistical robustness and histogram bin width selection.

ACKNOWLEDGMENTS

We gratefully acknowledge the financial support from the National Science Foundation (NSF) (Grant Nos. EEC-1941583 and ECCS-2407727), the Defense Advanced Research Projects Agency (DARPA) (Grant No. HR0011-24-2-0360), the Air Force Office of Scientific Research (AFOSR) (Grant No. FA955024PB004), the Naval Air Warfare Center Aircraft Division (Grant No. N6833522C0413), the Air Force Life Cycle Management Center (Grant No. FA8702-15-D-0001), the National Research Foundation of Korea (NRF) (Grant No. NRF-2022M3K4A1094782), and the Amazon Web Services (AWS) (Grant Nos. A50791 and A60290).

The authors also acknowledge the Harvard University Center for Nanoscale Systems (CNS) for providing the facilities used for device fabrication.

AUTHOR DECLARATIONS

Conflict of Interest

M.L. is a co-founder of a company that works on thin-film lithium niobate. The authors declare no other competing interests.

Author Contributions

X.Z. conceived the project, developed the device concept and experimental plan, performed the design, fabrication, measurements, and data analysis, and prepared the manuscript with input from all authors. H.W. assisted with device fabrication and contributed to the development of the resonance-spectrum fitting framework. Y.S. assisted with the optical measurements and led the development of the MZI-based wavelength calibration code. D.W. assisted with the HSQ dose optimization experiments. M.L. supervised the project and provided guidance on the research direction and the manuscript.

Xinrui Zhu: Conceptualization (equal); Formal analysis (equal); Investigation (equal); Methodology (equal); Visualization (equal); Writing – original draft (equal); Writing – review & editing (equal). **Hana K. Warner**: Formal analysis (supporting); Investigation (supporting); Writing – review & editing (supporting). **Yunxiang Song**: Investigation (supporting); Writing – review & editing (supporting). **Donald Witt**: Investigation (supporting). **Marko Lončar**: Funding acquisition (equal); Supervision (equal); Writing – review & editing (equal).

DATA AVAILABILITY

The data that support the findings of this study are available from the corresponding author upon reasonable request.

REFERENCES

[1] D. Zhu, L. Shao, M. Yu, R. Cheng, B. Desiatov, C. J. Xin, Y. Hu, J. Holzgrafe, S. Ghosh, A. Shams-Ansari, E. Puma, N. Sinclair, C. Reimer, M. Zhang, and M. Lončar, "Integrated photonics on thin-film lithium niobate," Adv. Opt. Photonics **13**, 242–352 (2021).

[2] A. Boes, L. Chang, C. Langrock, M. Yu, M. Zhang, Q. Lin, M. Lončar, M. Fejer, J. Bowers, and A. Mitchell, "Lithium niobate photonics: Unlocking the electromagnetic spectrum," Science **379**, eabj4396 (2023).

[3] Y. Hu, D. Zhu, S. Lu, X. Zhu, Y. Song, D. Renaud, D. Assumpcao, R. Cheng, C. J. Xin, M. Yeh, H. Warner, X. Guo, A. Shams-Ansari, D. Barton, N. Sinclair, and M. Loncar, "Integrated electro-optics on thin-film lithium niobate," Nat. Rev. Phys. **7**, 237–254 (2025).

[4] C. Wang, M. Zhang, X. Chen, M. Bertrand, A. Shams-Ansari, S. Chandrasekhar, P. Winzer, and M. Lončar, "Integrated lithium niobate electro-optic modulators operating at CMOS-compatible voltages," Nature **562**, 101–104 (2018).

[5] M. Xu, Y. Zhu, F. Pittalà, J. Tang, M. He, W. C. Ng, J. Wang, Z. Ruan, X. Tang, M. Kuschnerov, L. Liu, S. Yu, B. Zheng, and X. Cai, "Dual-polarization thin-film lithium niobate in-phase quadrature modulators for terabit-per-second transmission," Optica **9**, 61–62 (2022).

[6] J. Holzgrafe, N. Sinclair, D. Zhu, A. Shams-Ansari, M. Colangelo, Y. Hu, M. Zhang, K. K. Berggren, and M. Lončar, "Cavity electro-optics in thin-film lithium niobate for efficient microwave-to-optical transduction," Optica **7**, 1714–1720 (2020).

[7] H. K. Warner, J. Holzgrafe, B. Yankelevich, D. Barton, S. Poletto, C. J. Xin, N. Sinclair, D. Zhu, E. Sete, B. Langley, E. Batson, M. Colangelo, A. Shams-Ansari, G. Joe, K. K. Berggren, L. Jiang, M. J. Reagor, and M. Lončar, "Coherent control of a superconducting qubit using light," Nat. Phys. **21**, 831–838 (2025).

[8] T. P. McKenna, H. S. Stokowski, V. Ansari, J. Mishra, M. Jankowski, C. J. Sarabalis, J. F. Herrmann, C. Langrock, M. M. Fejer, and A. H. Safavi-Naeini, "Ultra-low-power second-order nonlinear optics on a chip," Nat. Commun. **13**, 4532 (2022).

[9] C. J. Xin, S. Lu, J. Yang, A. Shams-Ansari, B. Desiatov, L. S. Magalhães, S. S. Ghosh, E. McGee, D. Renaud, N. Achuthan, A. Zvyagintsev, D. Barton III, N. Sinclair, and M. Lončar, "Wavelength-accurate and wafer-scale process for nonlinear frequency mixers in thin-film lithium niobate," Commun. Phys. **8**, 136 (2025).

[10] Y. He, Q.-F. Yang, J. Ling, R. Luo, H. Liang, M. Li, B. Shen, H. Wang, K. Vahala, and Q. Lin, "Self-starting bi-chromatic $LiNbO_3$ soliton microcomb," Optica **6**, 1138–1144 (2019).

[11] Y. Song, X. Zhu, X. Zuo, G. Huang, and M. Lončar, "Stable gigahertz- and mmWave-repetition-rate soliton microcombs on X-cut lithium niobate," Optica **12**, 693–701 (2025).

[12]B. Nie, X. Lv, C. Yang, R. Ma, K. Zhu, Z. Wang, Y. Liu, Z. Xie, X. Jin, G. Zhang, D. Qian, Z. Chen, Q. Luo, S. Kang, G. Lv, Q. Gong, F. Bo, and Q.-F. Yang, "Soliton microcombs in X-cut $LiNbO_3$ microresonators," eLight **5**, 15 (2025).
[13]M. Zhang, B. Buscaino, C. Wang, A. Shams-Ansari, C. Reimer, R. Zhu, J. M. Kahn, and M. Lončar, "Broadband electro-optic frequency comb generation in a lithium niobate microring resonator," Nature **568**, 373–377 (2019).
[14]Y. Song, Y. Hu, X. Zhu, K. Powell, L. Magalhães, F. Ye, H. K. Warner, S. Lu, X. Li, D. Renaud, N. Lippok, D. Zhu, B. Vakoc, M. Zhang, N. Sinclair, and M. Lončar, "Integrated electro-optic digital-to-analogue link for efficient computing and arbitrary waveform generation," Nat. Photonics **19**, 1107–1115 (2025).
[15]Y. Hu, Y. Song, X. Zhu, X. Guo, S. Lu, Q. Zhang, L. He, C. A. A. Franken, K. Powell, H. Warner, D. Assumpcao, D. Renaud, Y. Wang, L. Magalhães, V. Rosborough, A. Shams-Ansari, X. Li, R. Cheng, K. Luke, K. Yang, G. Barbastathis, M. Zhang, D. Zhu, L. Johansson, A. Beling, N. Sinclair, and M. Lončar, "Integrated lithium niobate photonic computing circuit based on efficient and high-speed electro-optic conversion," Nat. Commun. **16**, 8178 (2025).
[16]M. Zhang, C. Wang, R. Cheng, A. Shams-Ansari, and M. Lončar, "Monolithic ultra-high-Q lithium niobate microring resonator," Optica **4**, 1536–1537 (2017).
[17]A. Shams-Ansari, G. Huang, L. He, Z. Li, J. Holzgrafe, M. Jankowski, M. Churaev, P. Kharel, R. Cheng, D. Zhu, N. Sinclair, B. Desiatov, M. Zhang, T. J. Kippenberg, and M. Lončar, "Reduced material loss in thin-film lithium niobate waveguides," APL Photonics **7**, 081301 (2022).
[18]X. Zhu, Y. Hu, S. Lu, H. K. Warner, X. Li, Y. Song, L. Magalhães, A. Shams-Ansari, A. Cordaro, N. Sinclair, and M. Lončar, "Twenty-nine million intrinsic *Q*-factor monolithic microresonators on thin-film lithium niobate," Photonics Res. **12**, A63–A68 (2024).
[19]A. Khalatpour, L. Qi, M. M. Fejer, and A. H. Safavi-Naeini, "Roughness-limited performance in ultra-low-loss lithium niobate cavities," Adv. Opt. Mater. **14**, e02355 (2026).
[20]X. Ji, J. K. Jang, U. D. Dave, M. Corato-Zanarella, C. Joshi, A. L. Gaeta, and M. Lipson, "Exploiting ultralow loss multimode waveguides for broadband frequency combs," Laser Photonics Rev. **15**, 2000353 (2021).
[21]A. Yariv, "Critical coupling and its control in optical waveguide-ring resonator systems," IEEE Photonics Technol. Lett. **14**, 483–485 (2002).
[22]W. Bogaerts, P. De Heyn, T. Van Vaerenbergh, K. De Vos, S. Kumar Selvaraja, T. Claes, P. Dumon, P. Bienstman, D. Van Thourhout, and R. Baets, "Silicon microring resonators," Laser Photonics Rev. **6**, 47–73 (2012).
[23]M. Bache and R. Schiek, "Review of measurements of Kerr nonlinearities in lithium niobate: The role of the delayed Raman response," arXiv:1211.1721 [physics] (2012).
[24]Y. Xu, M. Shen, J. Lu, J. B. Surya, A. A. Sayem, and H. X. Tang, "Mitigating photorefractive effect in thin-film lithium niobate microring resonators," Opt. Express **29**, 5497 (2021).
[25]A. Kordts, M. H. P. Pfeiffer, H. Guo, V. Brasch, and T. J. Kippenberg, "Higher order mode suppression in high-Q anomalous dispersion SiN microresonators for temporal dissipative Kerr soliton formation," Opt. Lett. **41**(3), 452–455 (2016).
[26]S. M. Spillane, T. J. Kippenberg, O. J. Painter, and K. J. Vahala, "Ideality in a fiber-taper-coupled microresonator system for application to cavity quantum electrodynamics," Phys. Rev. Lett. **91**, 043902 (2003).
[27]M. H. P. Pfeiffer, J. Liu, M. Geiselmann, and T. J. Kippenberg, "Coupling ideality of integrated planar high-*Q* microresonators," Phys. Rev. Appl. **7**, 024026 (2017).
[28]M. Wang, Y. Lei, Z.-G. Hu, C. Lao, Y. Wang, X. Zhou, J. Li, Q.-F. Yang, and B.-B. Li, "Coupling ideality of standing-wave supermode microresonators," Photonics Res. **12**, 1610 (2024).
[29]J. Liu, G. Huang, R. N. Wang, J. He, A. S. Raja, T. Liu, N. J. Engelsen, and T. J. Kippenberg, "High-yield, wafer-scale fabrication of ultralow-loss, dispersion-engineered silicon nitride photonic circuits," Nat. Commun. **12**, 2236 (2021).
[30]X. Ji, F. A. S. Barbosa, S. P. Roberts, A. Dutt, J. Cardenas, Y. Okawachi, A. Bryant, A. L. Gaeta, and M. Lipson, "Ultra-low-loss on-chip resonators with sub-milliwatt parametric oscillation threshold," Optica **4**, 619 (2017).